PAPER

Check for updates

Acid-activation enhanced graphite additive manufactured polypropylene sensor for the detection of parathion in forensic and environmental samples

Karen K. L. Augusto, [ID]†[ab] Larissa M. A. Melo, [ID]†[ac] Elena Bernalte,[a] Robert D. Crapnell, [ID][a] Rodrigo A. A. Muñoz, [ID][d] Orlando Fatibello-Filho, [ID][b] Wallans T. P. dos Santos [ID][ce] and Craig E. Banks [ID]*[a]

Parathion is a widely used pesticide that also acts as a hazardous toxicant, making its *in situ* detection crucial in both environmental and forensic contexts. As such, this study presents the development and application of a new additive manufactured electrodes composed of polypropylene (PP), carbon black (CB), and nitric acid-treated graphite (Gr(HNO$_3$)) for the electroanalytical detection of parathion. The physicochemical properties of the CB–Gr(HNO$_3$)/PP additive manufactured electrodes were thoroughly characterised using X-ray photoelectron spectroscopy (XPS), scanning electron microscopy (SEM), and Raman spectroscopy. Electrochemical characterisation revealed that introducing acid-treated graphite component significantly enhanced the electrode's electrochemical properties compared to untreated graphite electrodes. The electroanalytical performance of the CB–Gr(HNO$_3$)/PP electrode was subsequently assessed for the detection of parathion using adsorptive stripping square-wave voltammetry (SWAdSV), exhibiting a highly sensitive response, with a theoretical detection limit of 0.17 nM and a linear concentration range from 20 to 100 μM. The method demonstrated excellent reproducibility (RSD < 4%) and selectivity, with minimal interference from common contaminants. Parathion detection was successfully validated in real samples, showing recovery values of 91.5% in river water, 105.5% in urine, 76.9% in saliva, 102.9% in vitreous humour, and 87.6% in serum. It is demonstrated that the proposed CB–Gr(HNO$_3$)/PP electrode provides an effective platform for parathion sensing, highlighting the potential of additive manufacturing in advancing real-world analytical applications for environmental and forensic monitoring.

1. Introduction

Parathion is an important molecule used within agricultural insecticides, providing effective crops' protection against a broad spectrum of pests. However, its extensive agricultural application leads to environmental contamination through runoff and leaching, resulting in its presence within environmental waters.[1] To mitigate potential risks, the European Union has established a maximum permissible concentration of parathion in groundwater of 0.1 μg L^{-1} (0.34 nM).[2] Beyond its environmental impact, parathion is also a highly toxic substance to other non-target organisms and humans,[3] in which parathion inhibits acetylcholinesterase, an essential enzyme for correct nerve function. The accumulation of acetylcholine results in continuous signal transmission by the nerves, producing symptoms such as muscle twitching, respiratory distress, and convulsions.[1] Due to the rapid onset of these symptoms upon oral ingestion, parathion poisoning is often fatal, with real case studies reporting parathion concentrations in biological samples ranging from 8.3 to 68.6 μM.[4–7]

Given the serious environmental and toxicological implications of parathion exposure, many laboratory methods have been reported for its detection, including gas

[a] *Faculty of Science and Engineering, Manchester Metropolitan University, Dalton Building, Chester Street, M1 5GD, Great Britain, UK. E-mail: c.banks@mmu.ac.uk; Tel: +44 (0)1612 471196*

[b] *Department of Chemistry, Federal University of São Carlos, 13560-970, São Carlos, São Paulo, Brazil*

[c] *Department of Chemistry, Federal University of Vales do Jequitinhonha and Mucuri, Campus JK, 39100000, Diamantina, Minas Gerais, Brazil*

[d] *Institute of Chemistry, Federal University of Uberlândia, 38400-902, Uberlândia, Minas Gerais, Brazil*

[e] *Department of Pharmacy, Federal University of Vales do Jequitinhonha and Mucuri, Campus JK, 39100000, Diamantina, Minas Gerais, Brazil*

† These authors contributed equally to the work.

chromatography–mass spectrometry (GC–MS),[8–10] high-performance liquid chromatography–mass spectrometry (HPLC–MS),[11–13] and fluorescence spectroscopy.[14–16] Although sensitive, selective and reliable, these methods are all laboratory-based and require expensive equipment and skilled personnel as well as extensive sample collection, transportation and preparation, which are overall timely and costly procedures. To address this limitation, the development of low-cost, portable sensing platforms is required for *in situ* analysis of parathion in both environmental and forensic applications. Electrochemistry has demonstrated the potential to solve these issues due to its affordability, simplicity and ability to provide real-time analysis compared to gold-standard technologies. At the same time, with the advancement of high-performing, portable potentiostats, electrochemistry offers a viable solution for on-site analysis.

Electrochemical methods have been reported for the detection of parathion[17–20] with researchers using various electrodes, including hanging-drop mercury,[21] boron-doped diamond,[22] glassy carbon,[23] modified glassy carbon,[24] basal-plane pyrolytic graphite,[25] carbon paste,[26] screen-printed graphite,[27–29] and additive manufactured.[30,31] Among these, screen-printed electrodes (SPEs) and additive manufactured electrodes offer excellent synergy with *in situ* electroanalysis due to their cost-effectiveness, customisable designs and disposable nature, importantly eliminating the need for post-use surface replenishment. Although SPEs have been extensively studied with various modifications for parathion detection, very few studies have explored additive manufactured electrodes, with the only reports using commercially available conductive filament.[30,31]

The rise of additive manufacturing electrochemistry in recent years has been driven by its low-cost, rapid prototyping capabilities, and material versatility. Commercial conductive filament is available for fused filament fabrication (FFF), and is commonly used for sensor development throughout the literature,[32,33] but its performance is often severely limited by poor conductivity and solution ingress.[34] As such, researchers have begun developing bespoke conductive filaments,[35] where improvements in the sustainability[36] of filaments has been achieved through the use of bio-based plasticisers[37] or through utilisation of recycled PLA.[38,39] At the same time, electrochemical performance improvements have been achieved by combining synergetic carbon morphologies[40–44] or through changing the base polymer of the filament to improve electrode stability.[45–49]

A reported strategy for improving electrochemical performance of the additive manufactured electrodes involves combining graphite and carbon black, which enhances conductivity while reducing material costs.[40,41,47,50] One approach to further improve the electrochemical performance of graphite is activation, typically achieved *via* electrochemical, thermal, or chemical treatments. Therefore, in this work, we explore chemical activation with nitric acid

of graphite component to improve the performance of the bespoke conductive filament. Due to the acidic nature of the resultant graphite, polypropylene was chosen as the base polymer for filament production due to the susceptibility of PLA to chemical hydrolysis.[51] This activated-graphite polypropylene filament was then applied to the detection of parathion in both environmental and forensic samples, demonstrating how custom filament development can help advancing in the performance and applicability of additive manufacturing in electrochemical sensing.

2. Experimental

2.1. Chemicals and samples

Solutions were prepared using deionised water with an electric resistivity of ≥ 18.2 MΩ cm, obtained from a Milli-Q Integral 3 system (Millipore UK, Watford, UK). Hexaammineruthenium(III) chloride (98%), potassium ferricyanide (99%), potassium ferrocyanide (98.5–102%), boric acid ($\geq 99.5\%$), phosphoric acid (85%), acetic acid ($\geq 99.7\%$), sulphuric acid (99.999%), hydrochloric acid (37%), sodium hydroxide (>98%), nitric acid (70%), and potassium chloride (99.0–100.5%), uric acid (UA, $\geq 99\%$), ascorbic acid (AA, $\geq 99\%$), citric acid (CA, $\geq 98\%$), oxalic acid (OA, $\geq 99\%$) and caffeine (CAF, 99%), were acquired from Merck (Gillingham, United Kingdom). Carbon black was purchased from PI-KEM (Tamworth, United Kingdom), graphite powder (<53 μm) was purchased from Inoxia Ltd (Cranleigh, United Kingdom), and polypropylene (PP, Sabic® CX03-81 Natural 00,900) was purchased from Hardie Polymers (Glasgow, United Kingdom). The analytical standard of ethyl-parathion in liquid form, sourced from Tokyo Chemical Industry (Zwijndrecht, Belgium), was initially dissolved in methanol at a concentration of 1.0 mmol L^{-1} and subsequently diluted in appropriate supporting electrolytes for electrochemical analysis.

A Britton–Robinson (BR) buffer solution (0.1 M) was prepared using boric, phosphoric, and acetic acids, with sodium hydroxide (1.0 M) used to adjust the pH values between 2.0 and 12.0. Additionally, buffer solutions of nitric acid, hydrochloric acid, sulphuric acid, and BR (0.1 M) at pH 2.0 were evaluated as supporting electrolytes for parathion detection. Various nitric acid concentrations (0.05, 0.1, and 0.2 M) were also tested to assess the influence of ionic strength. Sodium hydroxide (NaOH) solution (0.5 M) was employed for the electrochemical activation of the working electrode.

Synthetic urine was produced according to the method described by Laube *et al.*,[52] artificial saliva as per Qian *et al.*,[53] and artificial vitreous humour according to Thakur *et al.*[54] In addition to synthetic biological samples, river water samples were collected in accordance with EPA guidelines from the River Irwell (Greater Manchester, United Kingdom), were diluted in supporting electrolyte (10×) and spiked with 70 μM of parathion prior to analysis.

2.2. Graphite modification

The graphite powder (Gr) was treated with nitric acid (HNO_3) to enhance its surface properties.[55] Next, 100 mL of a 0.5 M HNO_3 solution was prepared and added to 25 g of graphite powder, followed by continuous stirring overnight. The mixture was then filtered, and the resulting solid was dried in an oven at 60 °C overnight. The treated graphite, designated as $Gr(HNO_3)$, was subsequently used for filament production.

2.3. Filament production

The filament was prepared by combining precise amounts of polypropylene (PP), carbon black (CB), and acid-treated graphite $Gr(HNO_3)$ in a 63 cm^3 chamber. Based on a previous optimisation,[47] all filaments in this study consisted of 60 wt% PP, 20 wt% CB, and 20 wt% $Gr(HNO_3)$. The components were mixed using a Thermo Haake Polydrive dynameter equipped with a Thermo Haake Rheomix 600 (Thermo-Haake, Germany) at 210 °C, employing Banbury rotors at 70 rpm for 5 minutes. Following mixing, the polymer composites were cooled to room temperature and subsequently granulated using a Rapid Granulator 1528 (Rapid, Sweden) to achieve a finer particle size. The granulated material was then processed through the hopper of an EX2 extrusion line (Filabot, VA, United States), which utilised a single-screw extruder set to a heat zone of 210 °C. The molten polymer was extruded through a 1.75 mm die head, drawn along an Airpath cooling line (Filabot, VA, United States), and collected on a spool. The resulting filament was then ready for use in additive manufacturing.

2.4. Additive manufacturing of the electrodes

All computer designs and 3MF files in this study were created using Fusion 360® (Autodesk®, CA, United States). These files were then sliced and converted into GCODE using PrusaSlicer (Prusa Research, Prague, Czech Republic). The electrodes were fabricated via fused filament fabrication (FFF) on a Prusa i3 MK3S+ (Prusa Research, Prague, Czech Republic). All electrodes were printed using a 0.6 mm nozzle with a nozzle temperature of 245 °C, an extrusion ratio of 1.6 (160%), 100% rectilinear infill,[4] a layer height of 0.15 mm, a print speed of 35 mm s^{-1}, and a bed temperature of 110 °C. To enhance adhesion between the polypropylene filament and the printing bed, a thin layer of Magigoo™ adhesive was applied to the printing surface before heating the bed.

2.5. Physicochemical characterisation

X-ray photoelectron spectroscopy (XPS) data were collected using an AXIS Supra (Kratos, UK) equipped with a monochromatic Al X-ray source (1486.6 eV) operating at 225 W and a hemispherical sector analyser. The system was run in fixed transmission mode with a pass energy of 160 eV for survey scans and 20 eV for region scans. The collimator was set to slot mode, providing an analysis area of approximately 700 × 300 μm. The FWHM of the Ag $3d_{5/2}$ peak, measured with a pass energy of 20 eV, was 0.613 eV. The binding energy scale was calibrated by setting the graphitic sp^2 C 1s peak to 284.5 eV; although this calibration is known to be flawed[56] it was used due to the lack of better alternatives, as only limited information was derived from absolute peak positions.

Scanning electron microscopy (SEM) micrographs were acquired using a Crossbeam 350 focused ion beam-scanning electron microscope (FIB-SEM) (Carl Zeiss Ltd., Cambridge, UK) equipped with a field emission electron gun. Secondary electron imaging was performed with a secondary electron secondary ion (SESI) detector. Samples were mounted on 12 mm diameter aluminium SEM pin stubs (Agar Scientific, Essex, UK) using 12 mm diameter adhesive carbon tabs (Agar Scientific, Essex, UK) and coated with a 5 nm layer of Au/Pd using a Leica EM ACE200 coating system prior to imaging.

Raman spectroscopy was conducted using a DXR Raman microscope (Thermo Scientific Inc., Waltham, MA, United Stated) equipped with a 532 nm laser and operated with OMNIC 9 software.

2.6. Electrochemical instrumental and apparatus

Voltammetric experiments were conducted using a PGSTAT 204 potentiostat (Metrohm Autolab BV, Utrecht, Netherlands), operated through NOVA 2.1 software. The electrochemical characterization of parathion was carried out with lab-produced CB–$Gr(HNO_3)$/PP 3D-printed electrodes in a lollipop shape (Ø 5 mm disc a connection stem of 8 mm length, 2 mm width and 1 mm thickness[57]), a nichrome wire counter electrode, and a saturated Ag|AgCl reference electrode.

Before each measurement, the CB–$Gr(HNO_3)$/PP was electrochemically activated using 0.5 M NaOH by chronoamperometry, applying +1.4 V and −1.0 V for 200 s each. The electrochemical studies were performed using cyclic voltammetry at CB–$Gr(HNO_3)$/PP with different pH and scan rate values. Parathion electrochemical detection was optimised using the adsorptive stripping square-wave voltammetry (SWAdSV) technique with 70 mV amplitude, 7 mV step potential, 25 Hz frequency and 1 min pre-accumulation time, as the optimum parameters.

3. Results and discussion

3.1. Acid treatment of graphite and physicochemical characterisation of printed electrodes

Graphite treated with acid undergoes oxidation, resulting in the incorporation of oxygen-containing functional groups such as carboxyl (–COOH), hydroxyl (–OH), and carbonyl (–C═O) on its surface. This modification enhances the material's hydrophilicity and reactivity, potentially improving its electrochemical performance by facilitating charge transfer.[58,59] In this context, graphite powder was treated with 0.5 M HNO_3 to induce chemical modifications on the graphite surface. To investigate these changes, Fig. S1 presents the XPS spectra of the graphite

powder before (Fig. S1A) and after (Fig. S1B) acid treatment, providing insights into the effects of modification. The XPS spectra reveal four distinct peaks at different binding energies, corresponding to the functional groups C–C/C–H, C–O, C=C, and O–C=O. Fig. S1 displays the C 1s spectra of the graphite materials, where a prominent asymmetric C=C peak is fitted at 284.5 eV, attributed to the X-ray photoemission of graphitic carbon.[60,61] The peak fitting yielded standard deviations of 1.266 for graphite powder and 1.955 for HNO$_3$-treated graphite Gr(HNO$_3$), enabling the estimation of atomic concentrations of these functional groups (Table S1). Notably, compared to untreated graphite, Gr(HNO$_3$) exhibited a higher O–C=O content (23% *vs.* 16%), indicating the incorporation of additional oxygen-containing functional groups as a result of the acid treatment. In agreement with these findings, the O 1s spectra (Fig. S1C and D) show an increase in signal intensity after acid treatment, confirming the incorporation of additional oxygen species.

The additive manufacturing filament composed of PP, CB, and Gr(HNO$_3$) was produced following the previously reported method,[47] as illustrated in Fig. 1A. Briefly, the materials were added to a rheomixer chamber and mixed at 210 °C for five minutes using Banbury rotors. The resulting mixture was then cooled, pelletised, and extruded to generate an electrically conductive filament. This filament exhibited excellent flexibility at room temperature (Fig. 1B) and a resistance of (425 ± 32) Ω over a 10 cm length, considerably lower than that of commercially available PLA, which exhibited resistance values ranging from 2–3 kΩ and

compared to other bespoke filaments reported in the literature, with resistances of (864 ± 54) Ω for a CB-PLA filament[37] and (710 ± 30) Ω for a PETg filament containing graphene, multi-walled carbon nanotubes, and carbon black.[45] These results highlight the superior electrical conductivity of the bespoke CB–Gr(HNO$_3$)/PP filament. However, it is worth highlighting that a previous study using a CB : graphite ratio of 50 : 50 with PP reported a resistance of (223 ± 12) Ω, which is significantly lower than the value obtained in this work.[47] This difference can be attributed to the acid-treatment process. According to the literature, the introduction of oxygen-containing functional groups increases the defect density in graphite and reduces the degree of graphitisation, leading to a decline in conductivity.[62] Additionally, this filament demonstrated exceptional printability, as evidenced by the successful fabrication of lollipop-shaped additive manufactured electrodes used throughout this work (Fig. 1C).

Once printed, the electrodes were physiochemically characterised. SEM images were captured to analyse the surface morphology of the CB–Gr(HNO$_3$)/PP electrodes. As shown in Fig. 2A, the electrode surface consists of a polymer matrix, with small structures extruding from the surface, corresponding to the morphology of carbon black. Additionally, a graphite flake is visible, indicating the presence of graphite within the composite structure.

The chemical composition of the CB–Gr(HNO$_3$)/PP electrodes was analysed using XPS (C 1s) and Raman spectroscopy. Fig. 2B and C present the C 1s spectra for non-activated (or as-printed) and electrochemically activated electrodes, respectively. To achieve an accurate spectral fit,
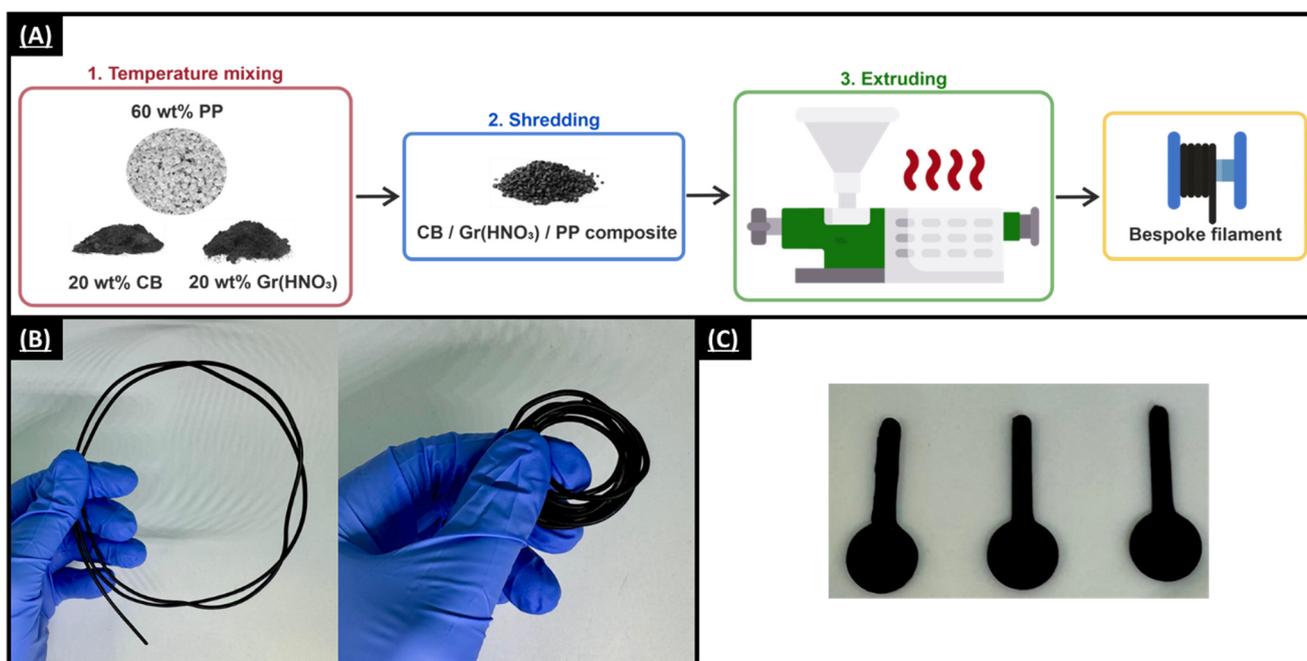

Fig. 1 (A) Schematic representation of filament production. (B) Photographs highlighting the low-temperature flexibility of the CB–Gr(HNO$_3$)/PP filament and (C) a picture of three additive-manufactured electrodes printed from this filament.
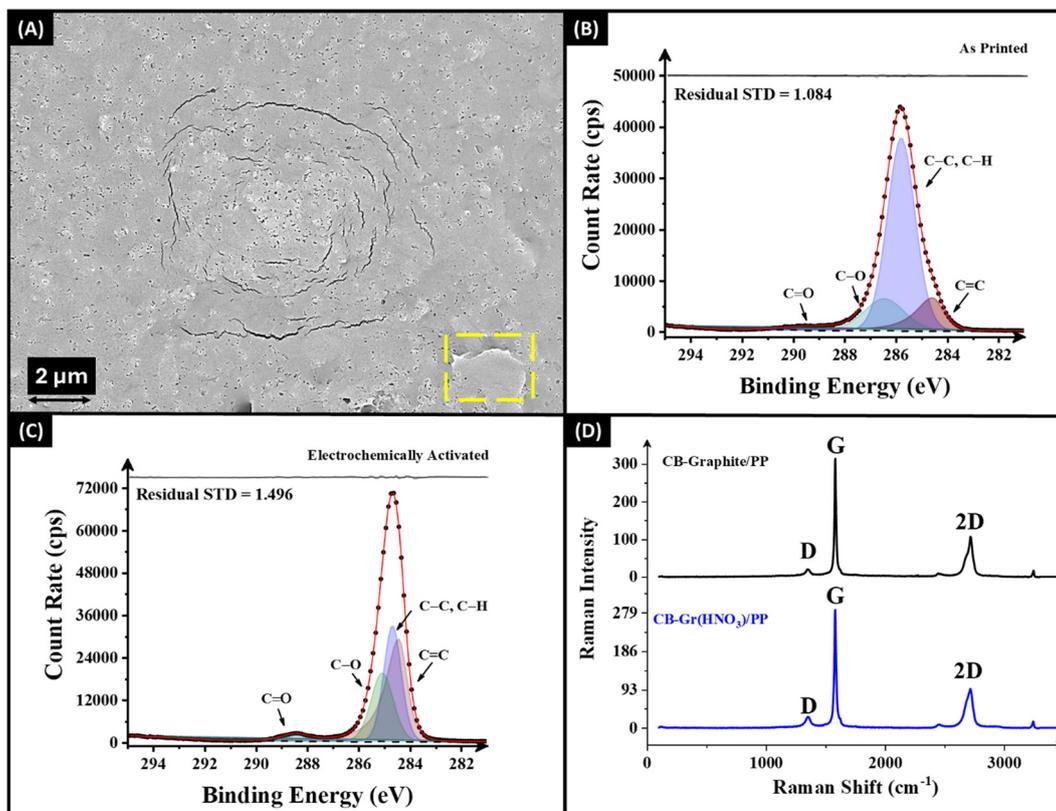
Fig. 2 (A) SEM image of the CB–Gr(HNO₃)/PP electrode after activation in 0.5 M NaOH. XPS C 1s spectra for the (B) as-printed and (C) electrochemically activated CB–Gr(HNO₃)/PP electrodes and (D) Raman spectra for the CB–graphite/PP and CB–Gr(HNO₃)/PP electrodes.

four peaks were assigned. The primary asymmetric peak at 284.5 eV corresponds to the X-ray photoemission of graphitic carbon.[60,61] Additionally, three symmetric peaks were required to fit the data, representing sp^3 C–C/C–H, C–O, and C=O bonding. In Fig. 2B, the dominant intensity of C–C bonding is expected due to the inherent structure of PP and the carbon fillers, while the C–O and C=O contributions originate from surface functionalities on both CB and Gr(HNO₃). In contrast, for the electrochemically activated CB–Gr(HNO₃)/PP electrode (Fig. 2C), the graphitic C=C peak increased, indicating greater exposure of conductive carbonaceous materials. Additionally, the intensities of the C–O and C=O bonds were enhanced, further supporting the increased accessibility of conductive sites.

Fig. 2D presents the Raman spectrum of the CB–graphite/PP (black line) and CB–Gr(HNO₃)/PP (blue line) electrodes, providing further insights into its chemical composition. Distinct peaks are observed at 1350, 1580, and 2720 cm^{-1}, corresponding to the characteristic D-, G-, and 2D-bands of graphitic structures. The I_D/I_G ratios are calculated as 0.066 for CB–graphite/PP and 0.095 for CB–Gr(HNO₃)/PP, indicating a lower defect density and a more ordered structure in the CB–graphite/PP electrode. The increase in the I_D/I_G ratio for CB–Gr(HNO₃)/PP suggests that acid treatment introduces more structural defects, leading to greater disorder within the graphitic structure.[62]

3.2. Electrochemical characterisation of the additive manufactured electrodes

The additive manufactured electrodes (CB–Gr(HNO₃)/PP) were characterised using common outer- and inner-sphere redox probes, $[Ru(NH_3)_6]^{3+}$ and $[Fe(CN)_6]^{4-/3-}$ (1.0 mM in 0.1 M KCl), as depicted in Fig. 3 and S2. As reported in a previous study,[47] electrochemical activation significantly enhances the electrode's electrochemical response by removing excess glue from the printing process. Therefore, all electrodes were electrochemically activated in 0.5 M NaOH using chronoamperometry, applying +1.4 V for 200 s followed by −1.0 V for 200 s. The electrochemical performance of the CB–Gr(HNO₃)/PP electrode was compared to that of the non-treated graphite electrode (CB–graphite/PP). Electrochemical characterisation was initially performed through scan rate studies using the $[Ru(NH_3)_6]^{3+}$ redox probe, as it provides the most reliable determination of the heterogeneous electron charge transfer rate constant (k^0) and the real electrochemical surface area (A_e).[63] The electroactive area was calculated using the Randles–Ševćik equation for quasi-reversible electrochemical systems,[63,64] eqn (1):

$$I_{p,f}^{quasi} = \pm 0.436 n F A_e C \sqrt{\frac{nFD\nu}{RT}} \qquad (1)$$

where n is the number of electrons involved in the electrochemical reaction, $I_{p,f}$ is the peak current corresponding
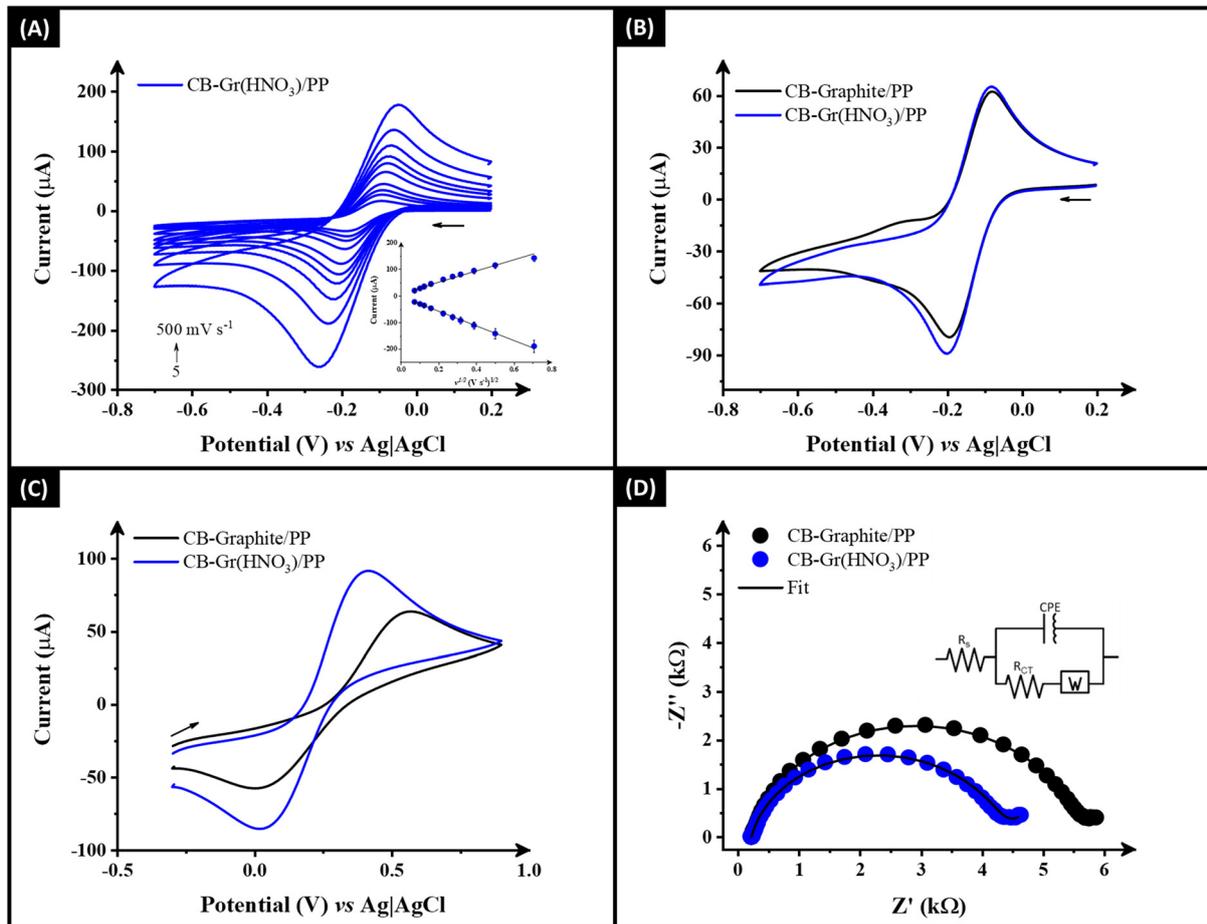
Fig. 3 (A) Scan rate study (5–500 mV s^{-1}) with [Ru(NH$_3$)$_6$]$^{3+}$ (1 mM in 0.1 M KCl) performed in the CB–Gr(HNO$_3$) as the WE. Inset: Randles–Ševčík plot. Cyclic voltammetry (50 mV s^{-1}) of (B) [Ru(NH$_3$)$_6$]$^{3+}$ and (C) [Fe(CN)$_6$]$^{4-/3-}$ comparing the electrodes. (D) EIS Nyquist plots of [Fe(CN)$_6$]$^{4-/3-}$ comparing the electrodes. Inset: the proposed equivalent circuit.

to the forward scan of the voltammetric response (analytical signal), C is the concentration of [Ru(NH$_3$)$_6$]$^{3+}$ in solution (mol cm^{-3}), F is the Faraday constant (C mol^{-1}), v is the scan rate (V s^{-1}), R is the universal gas constant (J mol^{-1} K^{-1}), T is the temperature in Kelvin (K), A_e is the electroactive surface area of the electrode (cm^2), and D is the diffusion coefficient of [Ru(NH$_3$)$_6$]$^{3+}$ (9.10 × 10^{-6} cm^2 s^{-1}). The k^0 was determined using the Nicholson method[65,66] using eqn (2), which is applicable to quasi-reversible electrochemical systems. For this, a potential scan rate study was conducted at scan rates ranging from 5 to 500 mV s^{-1}. Measurements were performed using the outer-sphere redox probe [Ru(NH$_3$)$_6$]$^{3+}$ in 0.1 M KCl.

$$\varphi = k^0 \left[\frac{\pi D n v F}{RT}\right]^{-1/2} \quad (2)$$

where φ is the kinetic parameter, and D, n, R, and T are as previously defined. The kinetic parameter φ is determined from the peak-to-peak separation obtained from cyclic voltammograms recorded at different scan rates. The k^0 is then calculated from the slope of the linear plot of φ vs

$(\pi D n v F/RT)^{-1/2}$. When ΔE_p exceeds 212 mV, the eqn (3) is applied, assuming an α of 0.5:[67]

$$k^0 = \left[2.18(\alpha D n v/RT)^{1/2}\right] e^{\left[-\left(\frac{\alpha^2 nF}{RT}\right) \times \Delta E_p\right]} \quad (3)$$

Fig. 3A shows a scan rate study for the CB–Gr(HNO$_3$)/PP electrode. The expected redox behaviour of [Ru(NH$_3$)$_6$]$^{3+}$ is observed, with well-defined one-electron reduction peaks at approximately −0.2 V. The inset in Fig. 3A presents the corresponding Randles–Ševčík plot, confirming the diffusion-controlled nature of the electrochemical process. The k^0 for the CB–Gr(HNO$_3$)/PP electrode was 2.3 (±0.1) × 10^{-3} cm s^{-1}, compared to 2.0 (±0.1) × 10^{-3} cm s^{-1}, slightly higher than that of the CB–graphite/PP electrode. Similarly, the real electrochemical surface area of the CB–Gr(HNO$_3$)/PP electrode was 0.36 (±0.05) cm^2, compared to 0.39 (±0.02) cm^2 for the CB–graphite/PP electrode.

The slight variations in k^0 and A_e, a comparison between the CB–Gr(HNO$_3$)/PP and CB–graphite/PP electrodes performed using cyclic voltammetry at 50 mV s^{-1} (Fig. 3B and C) shows that the CB–Gr(HNO$_3$)/PP electrode exhibited a peak-to-peak separation of 105 (±6) mV compared

© 2026 The Author(s). Published by the Royal Society of Chemistry

to 112 ($\pm$6) mV for CB–graphite/PP when using $[\text{Ru}(\text{NH}_3)_6]^{3+}$, and 360 ($\pm$24) mV compared to 476 ($\pm$32) mV when using $[\text{Fe}(\text{CN})_6]^{4-}/^{3-}$. Fig. 2B and 3C demonstrate significant enhancements in anodic (I_p^a) and cathodic peak currents (I_p^c) for the CB–Gr(HNO$_3$)/PP electrode compared to the CB–graphite/PP electrode, with increases of 1.12-fold and 1.44-fold in the I_p^a and I_p^c currents, respectively.

The additive manufactured electrodes were evaluated using electrochemical impedance spectroscopy (EIS) over a frequency range of 0.1 to 100 000 Hz against $[\text{Fe}(\text{CN})_6]^{4-/3-}$. EIS enables precise determination of the resistance introduced by the electrode through the calculation of the solution resistance (R_s) and the charge-transfer resistance (R_{CT}). The Nyquist plots for the additive manufactured electrodes printed from CB–Gr(HNO$_3$)/PP and CB–graphite/PP are shown in Fig. 3D. The CB–Gr(HNO$_3$)/PP electrode exhibited an R_s value of (215 ± 7) Ω, compared to (316 ± 11) Ω for the CB–graphite/PP electrode. The observed difference in R_s values is likely attributable to inconsistencies in cell assembly – specifically, variations in the spacing between electrodes-as the same electrolyte solution was employed in both cases. Additionally, the CB–Gr(HNO$_3$)/PP electrode showed a lower R_{CT} of (4.2 ± 0.3) kΩ compared to (5.3 ± 0.8) kΩ for CB–graphite/PP. These findings are consistent with the kinetic data obtained from cyclic voltammetric scan rate studies and further confirm the beneficial effects of nitric acid treatment on graphite. The significant improvements in kinetics and charge-transfer resistance highlight the enhanced electrochemical performance of CB–Gr(HNO$_3$)/PP over the untreated graphite filament. After electrochemical characterisation, the CB–Gr(HNO$_3$)/PP additive manufactured electrodes were utilised for the electroanalytical detection of parathion.

3.3. Electroanalytical determination of parathion

3.3.1 Electrochemical behaviour of parathion. The electrochemical behaviour of parathion was examined in a 0.1 M BR buffer solution across a pH range of 2.0 to 12.0 using cyclic voltammetry following the required NaOH activation of electrodes by chronoamperometry, as illustrated in Fig. S3. To avoid water oxidation in the anodic region and the subsequent appearance of an oxygen reduction peak in the solution, all voltammograms were initiated at 0 V with the initial scan directed toward the cathodic region. Parathion displays a quasi-reversible process (O$_1$/R$_2$) and an irreversible reduction process (R$_1$) at CB–Gr(HNO$_3$)/PP, as presented in Fig. S3 and S4. These processes exhibited pH-dependent behaviour, with peak potentials (E_p) shifting to more negative values as pH increased. Plots of peak potentials (E_p) and peak currents (I_p) for the redox processes as a function of pH at CB–Gr(HNO$_3$)/PP are shown in Fig. S5A and B and linear regressions for parathion redox processes are presented in Table S2. The obtained slopes of 0.052 V/pH for O$_1$/R$_2$ and 0.038 V/pH for R$_1$ are close to the theoretical value of 0.0592 V/pH (according to the Nernst
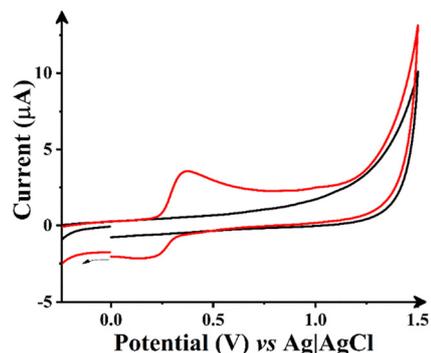

Fig. 4 Cyclic voltammetry of 100 μM parathion in 0.1 M nitric acid solution pH 2.0, at CB–Gr(HNO$_3$)/PP electrode. Scan rate: 50 mV s^{-1}.

equation) and approximately half of this value, respectively. These results indicate that equal numbers of electrons and protons are involved in the O$_1$/R$_2$ process, while in the R$_1$ process the number of electrons is twice the number of protons. Redox processes were observed only up to pH 7.0, which may be related to the molecule's pK_a (7.07),[28] suggesting that above this value, the molecule becomes protonated hindering the redox reaction.

In view of those results, for parathion detection, pH 2.0 was chosen, and various supporting electrolytes, namely BR buffer, nitric acid (HNO$_3$), hydrochloric acid (HCl), and sulphuric acid (H$_2$SO$_4$) were next evaluated, as shown in Fig. S6A. Interestingly, nitric acid yielded the most well-defined peaks and was therefore selected as the supporting electrolyte for parathion detection throughout this work. Then, different concentrations of nitric acid were tested to assess the effect of ionic strength in parathion detection, with 0.1 M nitric acid providing the best resolution of the observed redox processes (Fig. S6B). In Fig. 4 it is shown the electrochemical behaviour of parathion using the Gr(HNO$_3$)/PP electrode at the optimised pH and supporting electrolyte.

Later, cyclic voltammetry experiments at varying scan rates were performed to assess the mass transport control of parathion redox processes (O$_1$/R$_2$) on the CB–Gr(HNO$_3$)/PP surface (Fig. S7). The peak current (I_p) for parathion displayed a linear relationship with the square root of the scan rate ($v^{1/2}$) (Fig. S7B, $R^2 = 0.999$) and also with the scan rate (v) (Fig. S7D, $R^2 = 0.892$), indicating that the redox processes are controlled by both diffusion and adsorption at the CB–Gr(HNO$_3$)/PP surface. The logarithmic plot of I_p vs. logarithm of v show a linear relationship (Fig. S7C, $R^2 = 0.987$), following the regression equation: $\log I_p = -4.44$ ($\pm$0.04) + 0.71 ($\pm$0.03) $\log v$, with slope between 0.5 and 0.8, proving the mixed control (adsorption and diffusion) redox process for parathion on the developed sensor. Due to the adsorptive nature of this redox process, the Laviron equation (90.6/n mV) was applied,[68–70] and the number of electrons involved was estimated to be two. Furthermore, a proposed mechanism for the O$_1$, R$_1$, and R$_2$ processes of parathion at the CB–Gr(HNO$_3$)/PP electrodes was developed based on previous reports[71,72] and is presented in Scheme S1.
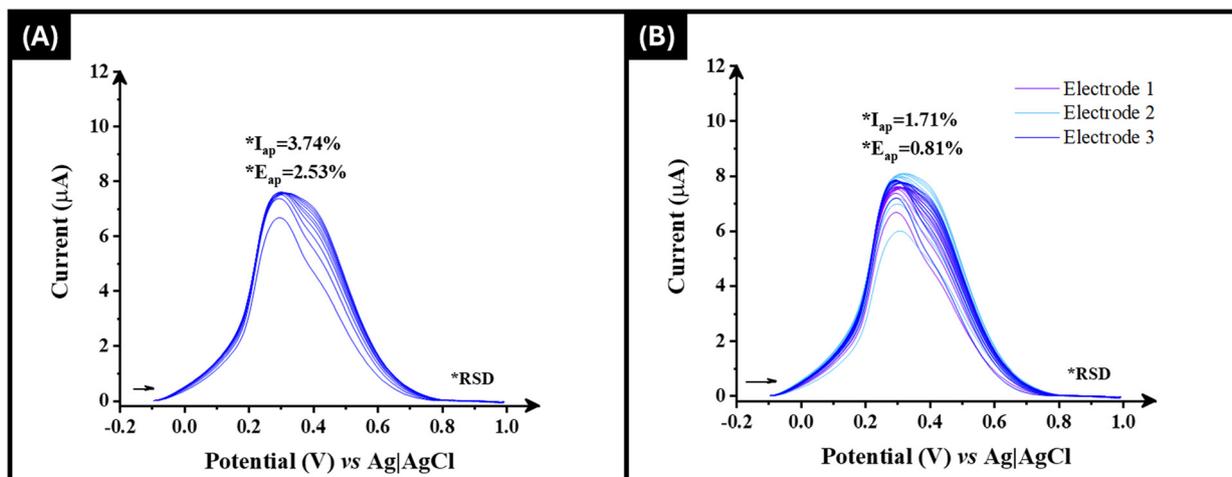
Fig. 5 SWAdSV voltammograms obtained for repetitive measurements ($N = 10$) in 0.1 M HNO_3 with 100 μM parathion using (A) one electrode and (B) three different CB–Gr(HNO_3)/PP electrodes as WE. All measurements were performed using the optimised conditions.

3.3.2 Parathion detection by SWAdSV using the CB–Gr(HNO_3)/PP electrode. Considering parathion's redox processes previously studied by cyclic voltammetry, a square-wave adsorptive stripping voltametric (SWAdSV) method was developed for more sensitive detection of parathion in real samples. Fig. S8 shows the effect of pre-accumulation time in CB–Gr(HNO_3)/PP for the detection of parathion. The I_p increased significantly up to 1 minute (see inset in Fig. S8); after this point, a saturation behaviour was observed. Using optimised conditions (70 mV amplitude, 7 mV step potential, 25 Hz frequency and 1 min pre-accumulation time), repeatability and reproducibility tests were first carried out using the same CB–Gr(HNO_3)/PP electrode ($N = 10$) and different electrodes ($N = 3$), for both studies respectively. The results obtained are shown in Fig. 5.

It can be seen that the proposed method exhibits good stability within the intra-electrode voltammetric responses for parathion (Fig. 5A), with low relative standard deviations (RSD) for E_p (<3%) and I_p (<4%). Similarly, the low standard deviations achieved inter-electrodes (Fig. 5B) demonstrate the good quality and reproducibility of the additive manufactured electrodes developed in this work. These results suggest that CB–Gr(HNO_3)/PP combined with SWAdSV is both an effective and promising screening approach for parathion detection. Thus, the linear working range for parathion determination was evaluated using standard solutions of the analyte ranging from 10 to 100 μM, as shown in Fig. 5.

Fig. 6 shows a linear range ($R^2 > 0.993$) for parathion quantification between 20 and 100 μM. Notably, a similar experiment was conducted on CB–graphite/PP electrodes without acid treatment, as shown in Fig. S9 highlighting a clear difference in sensitivity (0.023 μA μM^{-1}) between the electrodes. Linear regression equations for both electrodes are provided in Table S3, confirming that the acid treatment of graphite for filament production enhances the sensitivity (2.5-fold) for parathion detection. The results obtained in this

study were compared with those reported in the literature for the electrochemical detection of parathion (Table S4). The proposed sensor demonstrated satisfactory figures of merit relative to previously reported sensors. A key advantage of this approach lies in its straightforward fabrication process. Unlike several literature-reported methods that involve complex electrode modifications, the proposed AM electrodes are simpler to prepare and less labour-intensive.

To further illustrate this, parathion adsorption was characterised using the Langmuir isotherm (Fig. S10) and the rectangular box model (Scheme S1),[73–75] enabling the estimation of the actual surface area of CB–Gr(HNO_3)/PP electrode. It is estimated that the real surface area for CB–Gr(HNO_3)/PP electrodes is in the range between 0.445 and 0.639 cm^2, which is significantly larger than the surface area estimated for CB–graphite/PP between 0.175 and 0.251 cm^2, justifying the greater sensitivity shown by the CB–Gr(HNO_3)/PP electrode for the quantification of parathion molecule. The theoretical limits of detection (LOD) and quantification (LOQ) were calculated for both
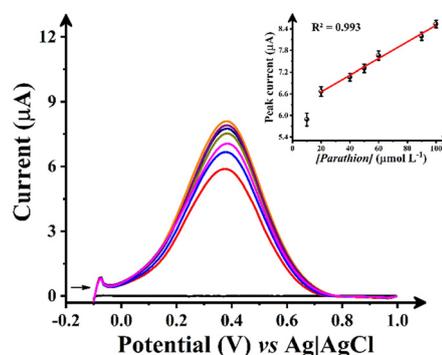

Fig. 6 SWAdSV voltammograms obtained for 0.1 M HNO_3 before (black line) and after addition of 10 to 100 μM parathion at CB–Gr(HNO_3)/PP. Inset: linear regression plot. All measurements were performed in triplicate using the optimised conditions.
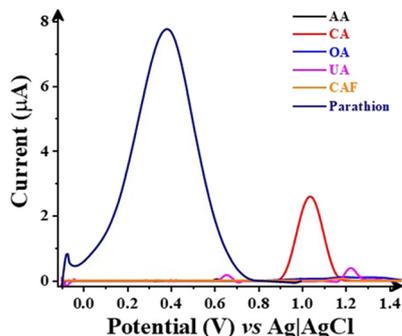
Fig. 7 SWAdSV voltammograms obtained for 0.1 M HNO_3 before and after addition of 1 mmol L^{-1} parathion (navy line), AA (black), CA (red), OA (blue), UA (magenta) and CAF (orange) at CB–Gr(HNO_3)/PP using the optimised parameters.

electrodes using the equations $3 \times S_B/m$ and $10 \times S_B/m$, where S_B represents the standard deviation of the blank response, and m is the slope of the regression line from the calibration curve. The LOD and LOQ values obtained for the CB–Gr(HNO_3)/PP electrode (0.17 and 0.56 nM) were significantly lower than the corresponding for the CB–graphite/PP electrode (0.48 and 1.62 nM), highlighting the enhanced sensitivity achieved through the acid treatment of the graphite powder prior to filament production. It is important to note that the calculated values are sufficiently low for real-sample applications. In forensic cases, biological samples typically exhibit high parathion concentrations in instances of attempted homicides and suicides, indicating intoxication. Real case studies have reported poisonings with parathion concentrations ranging from 8.3 to 68.6 μM,[4–7] which are significantly higher that our reported LOD and LOQ. In the case of environmental samples, the European Union has established a concentration of parathion in groundwater of 0.1 μg L^{-1} (0.34 nM),[2] It is important to highlight that, despite the low theoretical LOD and LOQ values indicating sufficient sensitivity for real applications in both forensic and environmental contexts, the lowest measurable

concentration in the calibration curve (Fig. 5 – red line) is 10 μM. A LOD value far below the first calibration point suggests an overly optimistic, theorical estimate derived from low background noise and an extrapolated slope rather than from the actual analytical performance, suggesting that the proposed method is more realistically suitable for forensic applications.

3.3.3 Electroanalytical determination of parathion in real samples. First, electroanalytical application of the CB–Gr(HNO_3)/PP electrode was performed in forensic matrixes. Therefore, to ensure the selective detection of parathion, the proposed method was tested against potential interferents that could be found in real samples of forensic interest. Voltammetric responses of ascorbic acid (AA), citric acid (CA), oxalic acid (OA). Uric acid (UA) and caffeine (CAF) were individually evaluated as well as parathion, as shown in Fig. 7.

It is clearly observed that AA, OA, and CAF did not exhibit any redox processes under the experimental conditions, therefore, no interferences are expected for parathion in the presence of these analytes. In contrast, CA displayed an oxidation peak at +1.04 V (*vs.* Ag|AgCl), while UA exhibited a peak at +1.21 V (*vs.* Ag|AgCl). However, despite these oxidation processes, the peak potentials of these compounds are sufficiently distant from the parathion peak potential (+0.38 V *vs.* Ag|AgCl), ensuring its selective identification at CB–Gr(HNO_3)/PP electrode.

Second, the electroanalytical application of parathion in synthetic biological samples (urine, saliva, serum, and vitreous humour) was performed together with an environmental river water sample. All samples were spiked with 70 μM parathion and quantification was performed using the external calibrations previously reported. Voltammetric responses are shown in Fig. 8 and the subsequent recovery values obtained are included in Table 1.

In all samples, the electrochemical profile observed after parathion addition was consistent with that of the parathion standard (Fig. 7), with all recoveries close to 100%, as detailed in Table 1. For the saliva sample, a lower recovery
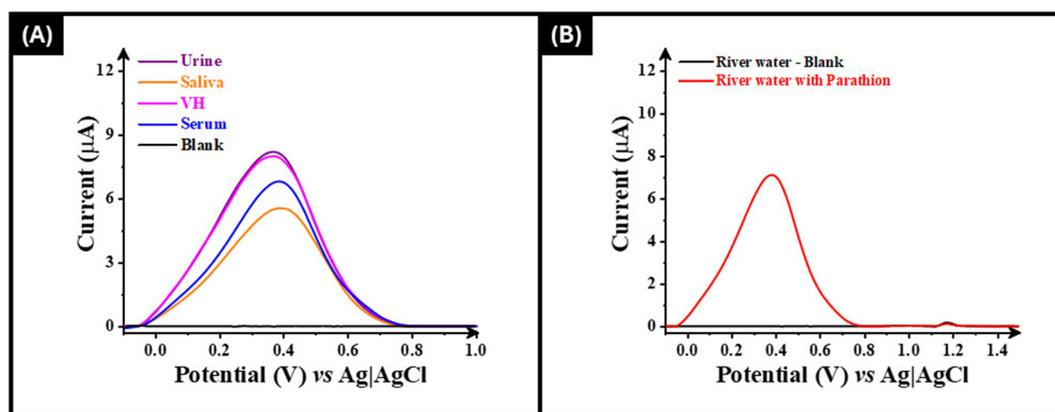

Fig. 8 SWAdSV voltammograms obtained for 0.1 mol L^{-1} HNO_3 before (black) and after addition of 70 μM parathion in (A) saliva (orange), vitreous humour (magenta), serum (blue), urine (purple) and (B) river water (red) at CB–Gr(HNO_3)/PP electrode using the optimised parameters.

Table 1 Recovery values (±RSD) for peak current (I_p) of 70 μM parathion in 0.1 M HNO_3 in biological and river water samples

Sample	Recovery
Urine	105.5 (±6.6) %
Saliva	76.9 (±5.3) %
Vitreous humour	102.9 (±5.0) %
Serum	87.6 (±1.2) %
River water	91.5 (±1.0) %

was obtained, likely due to the complexity of this matrix, indicating that the proposed method may not be appropriate for parathion quantification in saliva matrices. These findings indicate that SWAdSV with CB–Gr(HNO_3)/PP is minimally affected by the studied matrices. Thus, the proposed method demonstrates high efficiency for detecting parathion in forensic samples, such as biological specimens from attempted homicide/suicide cases, as well as in environmental samples for monitoring parathion contamination in water.

4. Conclusions

This study demonstrates the successful development of an additive manufactured electrode (CB–Gr(HNO_3)/PP) with enhanced electrochemical properties upon introducing acid-activated graphite for the detection of parathion, with applications in forensic investigations of parathion-related poisoning, attempted homicide, as well as environmental pollution scenarios. Compared to conventional additive manufactured electrodes made of CB and graphite, the incorporation of acid-treated graphite significantly improved the electrochemical properties of the electrode. These modifications contributed to a more efficient electron transfer process, leading to higher sensitivity and lower detection limits.

Using SWAdSV on a CB–Gr(HNO_3)/PP, parathion was rapidly and sensitively detected in biological and river water samples exhibiting excellent stability of the voltametric responses upon intra and inter-electrode measurements (RSD < 3% for E_p and < 4% for I_p). The quantification of parathion in the presence of potential interferents as well as in real biological and water samples with recovery values between 76.9 and 105.5% demonstrates that this approach offers a promising, rapid, and straightforward alternative for the analysis of parathion across different forensic and environmental matrices and highlights the advancements in additive manufacturing electrochemistry paving the way for future applications in the detection of hazardous compounds.

Conflicts of interest

There are no conflicts of interest to declare.

Data availability

Data is available from a request to the corresponding author.

Supplementary information (SI) is available. See DOI: https://doi.org/10.1039/d5sd00125k.

Acknowledgements

Notes and references

1 M. Richmond, in *Cancer Hazards: Parathion, Malathion, Diazinon, Tetrachlorvinphos and Glyphosate: The 2015 IARC Classifications: Implications for Regulation, Environmental Justice, and Global Health*, Springer, 2022, pp. 33–38.

2 M. Diagne, N. Oturan and M. A. Oturan, *Chemosphere*, 2007, **66**, 841–848.

3 F. Eyer, V. Meischner, D. Kiderlen, H. Thiermann, F. Worek, M. Haberkorn, N. Felgenhauer, T. Zilker and P. Eyer, *Toxicol. Rev.*, 2003, **22**, 143–163.

4 E. Bernalte, R. D. Crapnell, O. M. Messai and C. E. Banks, *ChemElectroChem*, 2024, **11**, e202300576.

5 G. K. Isbister, K. Mills, L. E. Friberg, M. Hodge, E. O'Connor, R. Patel, M. Abeyewardene and M. Eddleston, *Clin. Toxicol.*, 2007, **45**, 956–960.

6 H. Tsoukali, N. Raikos, G. Theodoridis and D. Psaroulis, *Forensic Sci. Int.*, 2004, **143**, 127–132.

7 D. W. Wyckoff, J. E. Davies, A. Barquet and J. H. Davis, *Ann. Intern. Med.*, 1968, **68**, 875–882.

8 D. F. da Silva, F. E. Paiva Silva, F. G. S. Silva, G. S. Nunes and M. Badea, *Pest Manage. Sci.*, 2015, **71**, 1497–1502.

9 J. Liu, L. Wang, L. Zheng, X. Wang and F. S. Lee, *J. Chromatogr. A*, 2006, **1137**, 180–187.

10 F. Musshoff, H. Junker and B. Madea, *Clin. Chem. Lab. Med.*, 1999, **37**, 639–642.

11 L. Chen, X. Dang, Y. Ai and H. Chen, *J. Sep. Sci.*, 2018, **41**, 3508–3514.

12 T.-T. Hu, C.-M. Lu, H. Li, Z.-X. Zhang, Y.-H. Zhao and J. Li, *Anal. Sci.*, 2017, **33**, 1027–1032.

13 Y. Huang, T. Shi, X. Luo, H. Xiong, F. Min, Y. Chen, S. Nie and M. Xie, *Food Chem.*, 2019, **275**, 255–264.

14 L. Liu, M. Qian, H. Sun, Z.-Q. Yang, L. Xiao, X. Gong and Q. Hu, *J. Food Compos. Anal.*, 2022, **107**, 104374.

15 X. Yan, H. Li, X. Wang and X. Su, *Talanta*, 2015, **131**, 88–94.

16 R. Zhang, L. Zhang, R. Yu and C. Wang, *Food Chem.*, 2023, **413**, 135679.

17 U. Jain, K. Saxena, V. Hooda, S. Balayan, A. P. Singh, M. Tikadar and N. Chauhan, *Food Chem.*, 2022, **371**, 131126.

18 H. Karimi-Maleh, R. Darabi, M. Baghayeri, F. Karimi, L. Fu, J. Rouhi, D. E. Niculina, E. S. Gündüz and E. Dragoi, *J. Food Meas. Charact.*, 2023, **17**, 5371–5389.

19 R. Ramachandran, V. Mani, S.-M. Chen, G. G. Kumar and M. Govindasamy, *Int. J. Electrochem. Sci.*, 2015, **10**, 859–869.

20 A. G.-M. Ferrari, R. D. Crapnell and C. E. Banks, *Biosensors*, 2021, **11**, 291.

21 J.-M. Zen, J.-J. Jou and A. S. Kumar, *Anal. Chim. Acta*, 1999, **396**, 39–44.

22 V. A. Pedrosa, D. Miwa, S. A. Machado and L. A. Avaca, *Electroanalysis*, 2006, **18**, 1590–1597.

23 Y. Yang, S. Chen, C. Zhang, Y. Li, X. Zong, Y. Lv and M. Zhang, *Anal. Methods*, 2024, **16**, 2522–2532.

24 D. Du, X. Ye and J. Zhang, *Electrochim. Acta*, 2008, **53**, 4478–4484.

25 L. L. Okumura, A. A. Saczk, M. F. d. Oliveira, A. C. C. Fulgêncio, L. Torrezani, P. E. N. Gomes and R. M. Peixoto, *J. Braz. Chem. Soc.*, 2011, **22**, 652–659.

26 P. R. de Oliveira, C. Kalinke, J. L. Gogola, A. S. Mangrich, L. H. M. Junior and M. F. Bergamini, *J. Electroanal. Chem.*, 2017, **799**, 602–608.

27 M. Govindasamy, V. Mani, S.-M. Chen, T.-W. Chen and A. K. Sundramoorthy, *Sci. Rep.*, 2017, **7**, 46471.

28 M. Khairy, H. A. Ayoub and C. E. Banks, *Food Chem.*, 2018, **255**, 104–111.

29 J. Mehta, P. Vinayak, S. K. Tuteja, V. A. Chhabra, N. Bhardwaj, A. K. Paul, K.-H. Kim and A. Deep, *Biosens. Bioelectron.*, 2016, **83**, 339–346.

30 B. C. Janegitz, R. D. Crapnell, P. Roberto de Oliveira, C. Kalinke, M. J. Whittingham, A. Garcia-Miranda Ferrari and C. E. Banks, *ACS Meas. Sci. Au*, 2023, **3**, 217–225.

31 Jyoti, E. Redondo, O. Alduhaish and M. Pumera, *Electroanalysis*, 2023, **35**, e202200047.

32 J. Fabri, L. R. Silva, J. S. Stefano, J. F. Pereira, D. R. Cocco, R. A. Muñoz and D. P. Rocha, *Microchem. J.*, 2023, **191**, 108810.

33 R. G. Rocha, D. L. Ramos, L. V. de Faria, R. L. Germscheidt, D. P. dos Santos, J. A. Bonacin, R. A. Munoz and E. M. Richter, *J. Electroanal. Chem.*, 2022, **925**, 116910.

34 R. J. Williams, T. Brine, R. D. Crapnell, A. G.-M. Ferrari and C. E. Banks, *Mater. Adv.*, 2022, **3**, 7632–7639.

35 R. D. Crapnell, C. Kalinke, L. R. G. Silva, J. S. Stefano, R. J. Williams, R. A. A. Munoz, J. A. Bonacin, B. C. Janegitz and C. E. Banks, *Mater. Today*, 2023, **71**, 73–90.

36 C. Kalinke, R. D. Crapnell, P. R. de Oliveira, B. C. Janegitz, J. A. Bonacin and C. E. Banks, *Glob. Chall.*, 2024, 2300408.

37 R. D. Crapnell, I. V. Arantes, M. J. Whittingham, E. Sigley, C. Kalinke, B. C. Janegitz, J. A. Bonacin, T. R. Paixão and C. E. Banks, *Green Chem.*, 2023, **25**, 5591–5600.

38 R. D. Crapnell, E. Sigley, R. J. Williams, T. Brine, A. Garcia-Miranda Ferrari, C. Kalinke, B. C. Janegitz, J. A. Bonacin and C. E. Banks, *ACS Sustainable Chem. Eng.*, 2023, **11**, 9183–9193.

39 E. Sigley, C. Kalinke, R. D. Crapnell, M. J. Whittingham, R. J. Williams, E. M. Keefe, B. C. Janegitz, J. A. Bonacin and C. E. Banks, *ACS Sustainable Chem. Eng.*, 2023, **11**, 2978–2988.

40 I. V. Arantes, R. D. Crapnell, E. Bernalte, M. J. Whittingham, T. R. Paixão and C. E. Banks, *Anal. Chem.*, 2023, **95**, 15086–15093.

41 K. K. Augusto, R. D. Crapnell, E. Bernalte, S. Zighed, A. Ehamparanathan, J. L. Pimlott, H. G. Andrews, M. J. Whittingham, S. J. Rowley-Neale and O. Fatibello-Filho, *Microchim. Acta*, 2024, **191**, 375.

42 R. D. Crapnell, I. V. Arantes, J. R. Camargo, E. Bernalte, M. J. Whittingham, B. C. Janegitz, T. R. Paixão and C. E. Banks, *Microchim. Acta*, 2024, **191**, 96.

43 M. Souza, R. G. Rocha, G. P. Siqueira, R. D. Crapnell, E. M. Richter, C. E. Banks and R. A. Muñoz, *Microchim. Acta*, 2025, **192**, 1–10.

44 M. M. Souza, G. P. Siqueira, R. G. Rocha, R. D. Crapnell, M. H. Santana, E. M. Richter, C. E. Banks and R. A. Muñoz, *J. Braz. Chem. Soc.*, 2024, **36**, e-20240186.

45 J. R. Camargo, R. D. Crapnell, E. Bernalte, A. J. Cunliffe, J. Redfern, B. C. Janegitz and C. E. Banks, *Appl. Mater. Today*, 2024, **39**, 102285.

46 R. D. Crapnell, E. Bernalte, E. Sigley and C. E. Banks, *RSC Adv.*, 2024, **14**, 8108–8115.

47 B. Ferreira, R. D. Crapnell, E. Bernalte, T. R. Paixão and C. E. Banks, *Electrochim. Acta*, 2025, **515**, 145680.

48 A. C. Oliveira, E. Bernalte, R. D. Crapnell, M. J. Whittingham, R. A. Munoz and C. E. Banks, *Appl. Mater. Today*, 2025, **42**, 102597.

49 D. L. Ramos, R. D. Crapnell, R. Asra, E. Bernalte, A. C. Oliveira, R. A. Muñoz, E. M. Richter, A. M. Jones and C. E. Banks, *ACS Appl. Mater. Interfaces*, 2024, **16**, 56006–56018.

50 K. K. Augusto, E. Bernalte, R. D. Crapnell, H. G. Andrews, O. Fatibello-Filho and C. E. Banks, *J. Environ. Chem. Eng.*, 2025, 116446.

51 M. A. Elsawy, K.-H. Kim, J.-W. Park and A. Deep, *Renewable Sustainable Energy Rev.*, 2017, **79**, 1346–1352.

52 N. Laube, B. Mohr and A. Hesse, *J. Cryst. Growth*, 2001, **233**, 367–374.

53 C. Qian, X. Wu, F. Zhang and W. Yu, *J. Prosthet. Dent.*, 2016, **116**, 112–118.

54 S. S. Thakur, S. K. Shenoy, J. S. Suk, J. S. Hanes and I. D. Rupenthal, *Eur. J. Pharm. Biopharm.*, 2020, **148**, 118–125.

55 B. Bowden, M. Davies, P. R. Davies, S. Guan, D. Morgan, V. Roberts and D. Wotton, *Faraday Discuss.*, 2018, **208**, 455–470.

56 G. Greczynski and L. Hultman, *Sci. Rep.*, 2021, **11**, 11195.

57 R. D. Crapnell, A. Garcia-Miranda Ferrari, M. J. Whittingham, E. Sigley, N. J. Hurst, E. M. Keefe and C. E. Banks, *Sensors*, 2022, **22**, 9521.

58 A. R. Cherian, L. Benny, A. George, A. Varghese and G. Hegde, *J. Nanostruct. Chem.*, 2021, 1–26.

59 A. Rehman, M. Park and S.-J. Park, *Coatings*, 2019, **9**, 103.

60 R. Blume, D. Rosenthal, J. P. Tessonnier, H. Li, A. Knop-Gericke and R. Schlögl, *ChemCatChem*, 2015, **7**, 2871–2881.

61 T. R. Gengenbach, G. H. Major, M. R. Linford and C. D. Easton, *J. Vac. Sci. Technol., A*, 2021, **39**, 013204.

62 C. Qiu, L. Jiang, Y. Gao and L. Sheng, *Mater. Des.*, 2023, **230**, 111952.

63 R. D. Crapnell and C. E. Banks, *Talanta Open*, 2021, **4**, 100065.

64 A. García-Miranda Ferrari, C. W. Foster, P. J. Kelly, D. A. C. Brownson and C. E. Banks, *Biosensors*, 2018, **8**, 53.

65 R. S. Nicholson, *Anal. Chem.*, 1965, **37**, 1351–1355.

66 S. J. Rowley-Neale, D. A. C. Brownson and C. E. Banks, *Nanoscale*, 2016, **8**, 15241–15251.

67 C. W. Foster, M. P. Down, Y. Zhang, X. Ji, S. J. Rowley-Neale, G. C. Smith, P. J. Kelly and C. E. Banks, *Sci. Rep.*, 2017, **7**, 42233.

68 E. Laviron, *J. Electroanal. Chem. Interfacial Electrochem.*, 1979, **101**, 19–28.

69 E. Laviron, *J. Electroanal. Chem. Interfacial Electrochem.*, 1974, **52**, 355–393.

70 E. Laviron and L. Roullier, *J. Electroanal. Chem. Interfacial Electrochem.*, 1980, **115**, 65–74.

71 T. Kokulnathan, T.-J. Wang and F. Ahmed, *J. Environ. Chem. Eng.*, 2021, **9**, 106537.

72 S. Sen, A. Roy, A. Sanyal and P. S. Devi, *Beilstein J. Nanotechnol.*, 2022, **13**, 730–744.

73 W. T. dos Santos and R. G. Compton, *Sens. Actuators, B*, 2019, **285**, 137–144.

74 L. M. Melo, L. C. Arantes, D. M. Pimentel, A. A. Macedo, R. M. Verly, E. S. Gil and W. T. dos Santos, *Sens. Actuators, B*, 2023, **393**, 134183.

75 L. M. Melo, L. C. Arantes, I. F. Schaffel, L. M. Aranha, N. S. Conceição, C. D. Lima, P. A. Marinho, R. Q. Ferreira and W. T. Dos Santos, *Analyst*, 2023, **148**, 1552–1561.